

## Interpretation of Unusual Absorption Bandwidths and Resonance Raman Intensities in Excited State Mixed Valence

Jenny V. Lockard, Guadalupe Valverde, Daniel Neuhauser, and Jeffrey I. Zink\*

Department of Chemistry and Biochemistry, University of California, Los Angeles, California 90095

Yun Luo, Michael N. Weaver, and Stephen F. Nelsen\*

Department of Chemistry, University of Wisconsin, 1101 University Avenue, Madison, Wisconsin 53706-1396

Received: October 14, 2005

Excited state mixed valence (ESMV) occurs in molecules in which the ground state has a symmetrical charge distribution but the excited state possesses two or more interchangeably equivalent sites that have different formal oxidation states. Although mixed valence excited states are relatively common in both organic and inorganic molecules, their properties have only recently been explored, primarily because their spectroscopic features are usually overlapped or obscured by other transitions in the molecule. The mixed valence excited state absorption bands of 2,3-di-*p*-anisyl-2,3-diazabicyclo[2.2.2]octane radical cation are well-separated from others in the absorption spectrum and are particularly well-suited for detailed analysis using the ESMV model. Excited state coupling splits the absorption band into two components. The lower energy component is broader and more intense than the higher energy component. The absorption bandwidths are caused by progressions in totally symmetric modes, and the difference in bandwidths is caused by the coordinate dependence of the excited state coupling. The Raman intensities obtained in resonance with the high and low energy components differ significantly from those expected based on the oscillator strengths of the bands. This unexpected observation is a result of the excited state coupling and is explained by both the averaging of the transition dipole moment orientation over all angles for the two types of spectroscopies and the coordinate-dependent coupling. The absorption spectrum is fit using a coupled two-state model in which both symmetric and asymmetric coordinates are included. The physical meaning of the observed resonance Raman intensity trends is discussed along with the origin of the coordinate-dependent coupling. The well-separated mixed valence excited state spectroscopic components enable detailed electronic and resonance Raman data to be obtained from which the model can be more fully developed and tested.

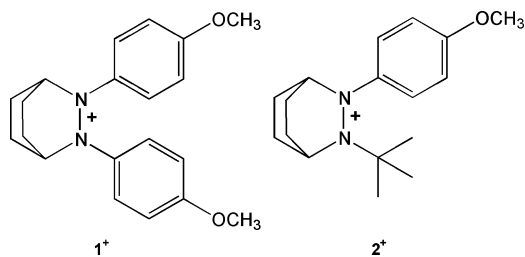
### Introduction

Some of the most commonly encountered molecular systems having a mixed valence excited state contain two identical charge-bearing units M separated by a bridge B, often denoted as M–B–M type systems. The ground electronic state for this class of intervalence systems has a symmetrical charge distribution, M–B<sup>+</sup>–M for example, while the excited electronic state possesses two or more interchangeably equivalent sites that have different oxidation states, M<sup>+</sup>–B–M/M–B–M<sup>+</sup>.<sup>1,2</sup> Unlike the absorption spectrum associated with ground state mixed valence, which consists of a single peak maximum at an energy equal to twice the coupling,<sup>3–9</sup> the absorption band resulting from an excited state mixed valence (ESMV) transition consists of two components separated in energy by twice the effective coupling in the excited state.

The first ESMV system that we studied, 1,4-bis(2-*tert*-butyl)-2,3-diazabicyclo[2.2.2]oct-3-yl)-2,3,5,6-tetramethylbenzene-1,4-diyl dication, consisted of a durene bridge B, para-substituted with hydrazine charge-bearing units, M.<sup>1</sup> The ground state charge distribution is symmetric, verified for the solid state by an X-ray crystal structure,<sup>10</sup> M<sup>+</sup>–B–M<sup>+</sup>, but the electronic transition transfers charge from one M to the other to produce two excited state configurations: M<sup>2+</sup>–B–M and M–B–M<sup>2+</sup>. The experimental absorption band assigned to the ESMV transition consists of a dominant band with an unresolved

shoulder. Recently, we reported the analysis of another ESMV system, 2,3-diphenyl-2,3-diazabicyclo[2.2.2]octane radical cation.<sup>2</sup> In this example, the charge-bearing units, M, in the excited state are the phenyl groups and the bridge, B, is the substituted hydrazine. In the ground state, the charge is located on the bridge, M–B<sup>+</sup>–M, and an one electron transition from the M units to the bridge gives rise to the mixed valence excited state, M<sup>+</sup>–B–M/M–B–M<sup>+</sup>. The absorption band resulting from this transition contains two components that are more resolved than the previous dication example but still contain significant overlap with each other and the next higher energy band. While the spectra of both reported examples of ESMV clearly contain the two characteristic absorption band components, their overlap with each other and other higher energy bands makes a detailed resonance Raman analysis difficult because resonance Raman intensities that occur when in resonance with each of these components are influenced by the interference between the two components and between these components and higher energy overlapping bands.<sup>11–19</sup>

The ESMV system studied in this work is 2,3-di-*p*-anisyl-2,3-diazabicyclo[2.2.2]octane radical cation, 1<sup>+</sup>. We designed this molecule such that the two absorption band components shown in Figure 1 have good energy separation from each other and from the next higher energy band. Because the lowest energy absorption band involves charge transfer from the aryl



groups to the  $(NN)^+ 3e-\pi$  bond, it is not surprising that electron-releasing substituents on the aryl groups lower the transition energy for this band. A survey of several p-substituted derivatives of the diphenyl compound showed that the dianisyl compound had the most favorable spectrum for resonance Raman analysis. Both components of the ESMV absorption band were substantially red shifted, from 18000 and  $\sim 24100\text{ cm}^{-1}$  of the phenyl-substituted compound to 15000 and  $20100\text{ cm}^{-1}$  for the anisyl-substituted one, accompanied by a substantial increase both in intensity of the ESMV band and in relative intensity of its higher energy component. The better resolution of the two absorption band components also reveals that they have different widths. These spectral changes greatly decrease the serious overlap of the ESMV band of the phenyl-substituted compound with the stronger  $NN(\pi,\pi^*)$  absorption near  $29000\text{ cm}^{-1}$ , allowing an accurate resonance Raman investigation of the coupled excited state. For an uncoupled system, resonance Raman intensities are expected to follow the intensity profile of the absorption spectrum. The Raman intensities obtained in resonance with the high and low energy absorption band components of  $1^+$ , however, differ significantly from the absorption intensity ratio.

In this paper, the unusual experimental spectroscopic results for  $1^+$  are analyzed using an ESMV model. The different intensity ratios of the absorption vs resonance Raman spectra are a consequence of the excited state coupling and the averaging of the transition dipole moment orientation over all angles to account for the random molecular orientations for the two types

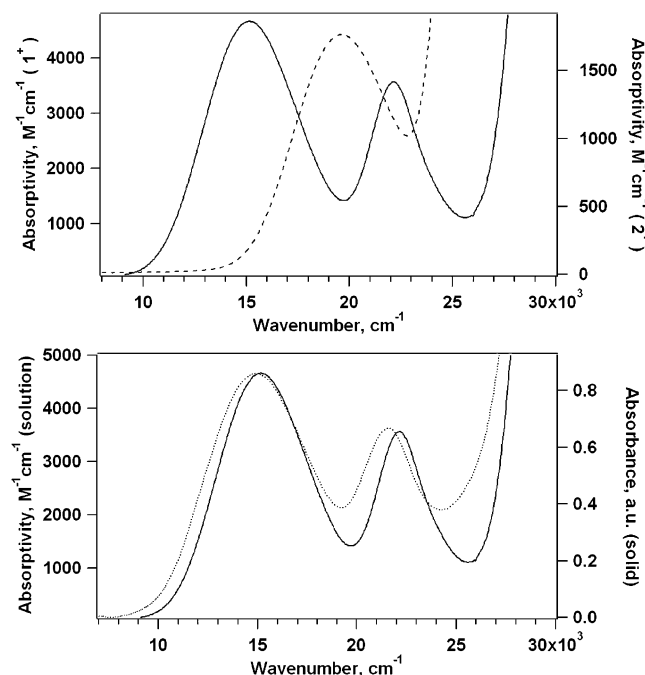


**Figure 1.** (Top panel) Absorption spectra of  $1^+$  (solid line) and  $2^+$  (dashed line) in acetonitrile solution. (Bottom panel) Absorption spectra of  $1^+$  in acetonitrile solution (solid line) and as a solid in a pressed KBr pellet (dotted line).

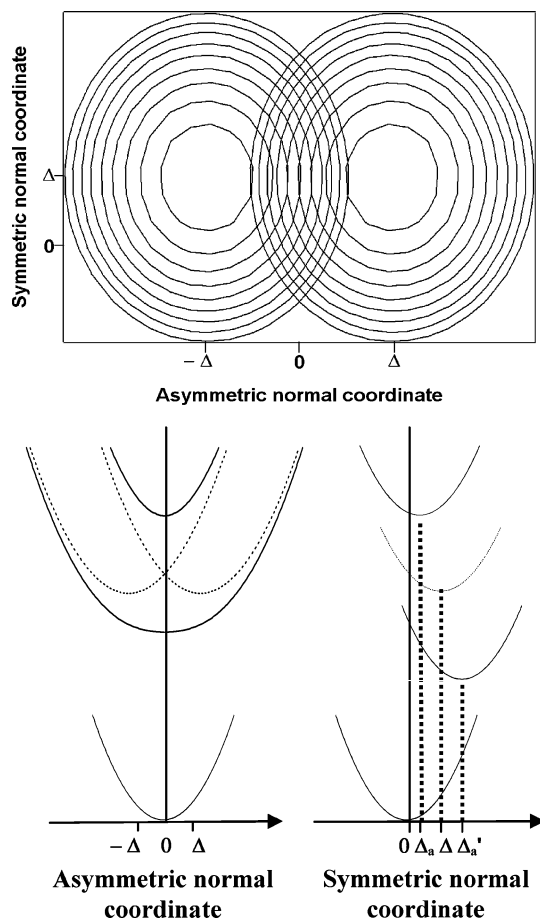


**Figure 2.** Ground and mixed valence excited state surfaces. (Top panel) A 2D contour plot of the excited state diabatic potential energy surfaces.  $\Delta$  indicates displacement of the surface minima from that of the ground state surface (defined as 0) along each coordinate. (Bottom panel) Cross-sections of the ground state, excited state diabatic (dotted), and excited-state adiabatic (solid) surfaces along the asymmetric (lower left) and symmetric (lower right) normal coordinates.  $\Delta$  is the displacement of the minima of the excited state diabatic surfaces along either the symmetric or the asymmetric coordinate.  $\Delta_a$  and  $\Delta'_a$  are the displacements of the upper and lower adiabatic surfaces, respectively, along the symmetric coordinate.

of spectroscopy. We derive the relationship between the orientation of transition dipole moments, the excited state coupling, and the intensity ratio of the two components of the absorption spectrum and resonance Raman profiles for the two spectroscopic processes. The theoretical resonance Raman intensity ratio resulting from the ESMV system with nonlinear transition dipoles is used to explain the observed resonance Raman intensity trends. The effect of coordinate-dependent coupling on bandwidth and relative intensities of these two types of spectra is also discussed and used to explain the observed spectroscopic results. The different widths of the two absorption band components are explained by a coordinate dependence of the effective excited state coupling. Electronic transitions to mixed valence excited states are treated quantitatively in this paper using the time-dependent theory of spectroscopy<sup>20–24</sup> specifically applied to coupled electronic states.<sup>25–34</sup> A fit to the absorption spectrum is calculated using the two-dimensional (2D) coupled two-state surface shown in Figure 2. A constant component of the effective coupling, which is positive, is the same along both coordinates and gives rise to the appropriate energy splitting of the two bands. A coordinate-dependent coupling is included along the symmetric coordinate to accom-

moderate the different bandwidths of the two absorption band components.

## Experimental Section

**Synthesis.** 2,3-Di(4'-methoxyphenyl)-2,3-diazabicyclo[2.2.2]octane. A solution containing 22 mmol of *t*-BuLi was added dropwise to a 100 mL Schlenk flask containing 60 mL of dry ether and *p*-bromoanisole (10 mmol) while stirring at  $-78\text{ }^{\circ}\text{C}$  under nitrogen. After addition, the dry ice-acetone bath was removed, and the reaction mixture was raised to room temperature, equipped with a condenser, and heated under reflux for 10 min. The mixture was allowed to cool to  $-78\text{ }^{\circ}\text{C}$ , and 10 mmol of 2,3-diaza-bicyclo[2.2.2]oct-2-ene<sup>35</sup> was added. After the reaction mixture was kept at  $-78\text{ }^{\circ}\text{C}$  for 0.5 h, it was raised to room temperature and kept at that temperature for 1 h. The reaction mixture was cooled to  $-78\text{ }^{\circ}\text{C}$  again, and 5 g of iodine in 30 mL of dry ether was added. After the dry ice-acetone bath was removed, it was stirred another hour under nitrogen, filtered, and washed several times with ether. This solid was dried at  $60\text{ }^{\circ}\text{C}$  under a reduced pressure for 24 h and added into 10 mmol of freshly made lithium anisyl at  $-78\text{ }^{\circ}\text{C}$ . After the cooling bath was removed, the mixture was stirred at room temperature for another 2 h. Water was added to quench the reaction, and the organic layer was collected. The aqueous solution was extracted with toluene three times. The extract was dried over  $\text{MgSO}_4$ , and the solvents were removed under reduced pressure. The solid was crystallized with ether/pentane to obtain 1.5 g (46%) of 2,3-dianisyl-2,3-diazabicyclo[2.2.2]-hydrazine; mp  $162\text{--}163\text{ }^{\circ}\text{C}$ .  $^1\text{H NMR}$  ( $\text{CD}_3\text{CN}$ ):  $\delta$  6.91 (d,  $J = 9.2\text{ Hz}$ , 4H), 6.75 (d,  $J = 9.3\text{ Hz}$ , 4H), 4.15 (s, 2H), 3.5 (s, 6H), 1.45–2.0 (m, 8H). The empirical formula  $\text{C}_{20}\text{H}_{24}\text{N}_2\text{O}_2$  was established by high-resolution MS.

2-*tert*-Butyl-3-(4'-methoxyphenyl)-2,3-diazabicyclo[2.2.2]octane. 2-*tert*-Butyl-2,3-diaza-bicyclo[2.2.2]oct-2-ene iodide<sup>36</sup> (1.5 mmol) was added to a freshly prepared 4-methoxyphenyllithium solution (1.5 mmol) while stirring at  $-78\text{ }^{\circ}\text{C}$  under nitrogen. After the solution was stirred at  $-78\text{ }^{\circ}\text{C}$  for 0.5 h and room temperature for 1 h, water was added to quench the reaction. The organic layer was collected, and the aqueous solution was extracted twice with toluene. The solid obtained after removal of the solvent was crystallized from ether/pentane to give 0.18 g (50.4%) of 2-*tert*-butyl-3-(4'-methoxyphenyl)-2,3-diaza-bicyclo[2.2.2]octane; mp  $68\text{--}69\text{ }^{\circ}\text{C}$ .  $^1\text{H NMR}$  ( $\text{CD}_3\text{CN}$ ):  $\delta$  7.75 (s, 1H), 6.91 (s, 1H), 6.75 (d,  $J = 9.3\text{ Hz}$ , 2H), 3.75 (s, 3H), 3.6 (s, 1H), 3.4 (s, 1H), 1.45–2.2 (m, 8H), 1.05 (s, 9H). The empirical formula  $\text{C}_{17}\text{H}_{26}\text{N}_2\text{O}$  was established by high-resolution MS.

**Solution of 2,3-Di(4'-methoxyphenyl)-2,3-diazabicyclo[2.2.2]octane Radical Cation.** Solid tris(*p*-bromophenylammonium hexafluorophosphate (8.1 mg,  $11.28\text{ }\mu\text{mol}$ ) and neutral hydrazine (3.9 mg,  $12.02\text{ }\mu\text{mol}$ ) were added to a 25 mL volumetric flask in a nitrogen-filled glovebag, and the mixture was diluted to 25 mL with freshly dried acetonitrile. A 1 mL aliquot was diluted to 10 mL in a volumetric flask, giving a  $45\text{ }\mu\text{M}$  solution of radical cation for absorption spectroscopy.

**Cation Solution of 2-*tert*-Butyl-3-(4'-methoxyphenyl)-2,3-diazabicyclo[2.2.2]octane.** A  $24.5\text{ }\mu\text{M}$  radical cation solution was prepared in the same manner from 4.4 mg of tris(*p*-bromophenylammonium hexafluorophosphate (6.13  $\mu\text{mol}$ ) and the neutral hydrazine (1.8 mg,  $6.55\text{ }\mu\text{mol}$ ).

**Solid 2,3-Di(4'-methoxyphenyl)-2,3-diazabicyclo[2.2.2]octane Radical Cation.** A mixture of oxidant (40.0 mg,  $55.72\text{ }\mu\text{mol}$ ) and hydrazine (19.0 mg,  $58.56\text{ }\mu\text{mol}$ ) was shaken under nitrogen with 1 mL of acetonitrile for 1 min, placed into an ethyl ether

atmosphere, and allowed to crystallize in a freezer for 2 weeks. After the mixture was filtered and washed with dry ether, solid  $1^+\text{PF}_6^-$  was obtained (11 mg, 35%).

**Absorption Spectroscopy.** Absorption spectra taken of acetonitrile solution samples at room temperature were obtained using a Perkin-Elmer Lambda 20 UV-vis spectrophotometer. Solid-state absorption spectra were obtained from a KBr pellet using a Cary 5000 UV-vis-nIR spectrophotometer.

**Raman Spectroscopy.** Spectra were obtained using a triple monochromator equipped with a Princeton Instruments LN-CCD. Data were processed by a PC computer. The 676 nm line of a Coherent I-300 Krypton laser and the 476 nm line of a Coherent Argon laser at  $\sim 100\text{ mW}$  were used for excitation. The spectra were collected from a solid sample of  $1^+$  in a spinning sodium nitrate pellet.

## Theoretical and Numerical Methods

The Gaussian 98 program suite was used for B3LYP/6-31G\* calculations,<sup>37,38</sup> and standard Pople style basis sets and all correlation methods were used as implemented within Gaussian 98. Geometry optimizations were performed using standard gradient methods. Frequency calculations were conducted on optimized geometries to confirm that a minimum had been located on the potential energy surface. Geometries obtained through Gaussian 98 calculations were viewed using the MOLDEEN software package for viewing vibrational motions.<sup>39</sup> Calculated vibrational modes were viewed using MOLDEEN and GaussView 2.0.

Electronic spectra for ESMV potential surfaces are calculated in the framework of the time-dependent theory of molecular spectroscopy. The theoretical foundation underlying these calculations has been described previously.<sup>20–24</sup> In this section, the theory underlying the calculation of absorption spectra and resonance Raman profiles for coupled potential surfaces is briefly presented.

**Absorption Spectra.** The fundamental equation for the calculation of an absorption spectrum in the time-dependent theory is

$$I(\omega) = C\omega \int_{-\infty}^{+\infty} \exp(i\omega t) \left\{ \langle \Phi | \Phi(t) \rangle \exp\left(-\Gamma^2 t^2 + \frac{iE_0}{h} t\right) \right\} dt \quad (1)$$

with  $I(\omega)$  the absorbance at frequency  $\omega$ ,  $E_0$  the energy of the electronic origin transition, and  $\Gamma$  a phenomenological Gaussian damping factor.<sup>24</sup> The damping factor arises because of relaxation into other modes (such as low frequency solvent modes with small distortions) and the “bath”. The effect of increasing  $\Gamma$  on the spectrum in the frequency domain is to decrease the resolution, that is, to “fill in” the spectrum. The most important part of eq 1 is  $\langle \Phi | \Phi(t) \rangle$ , the autocorrelation function of the wave packet  $\Phi$  prepared on excited state potential surfaces after the spectroscopic transition, with the wave packet  $\Phi(t)$  developing on these surfaces with time. In the absence of coupling terms between the normal coordinates, the total autocorrelation in a system with  $K$  coordinates is given by:

$$\langle \Phi | \Phi(t) \rangle = \prod_k \langle \phi^k | \phi^k(t) \rangle \quad (2)$$

where  $\phi^k$  is a wave packet associated with coordinate  $k$  ( $k = 1, \dots, K$ ) and is a 2D vector:  $\phi^k(Q_k, j)$ , where  $Q_k$  is the coordinate along mode  $K$ , and  $j = 1, 2$  is an index over the two electronic states. When two coupled surfaces that represent the excited state are involved, we need to keep track of two wave packets,

$\phi_1$  and  $\phi_2$  moving on the two coupled potential surfaces.<sup>40–45</sup> The wave packet  $\phi(t)$  is given by the time-dependent Schrödinger equation:

$$i \frac{\partial}{\partial t} \begin{pmatrix} \phi_1 \\ \phi_2 \end{pmatrix} = \begin{pmatrix} H_1 & H_{\text{eff}} \\ H_{\text{eff}} & H_2 \end{pmatrix} \begin{pmatrix} \phi_1 \\ \phi_2 \end{pmatrix} \quad (3)$$

(where the subscript denotes the electronic state,  $j = 1$  or  $2$ ).  $H_{\text{eff}}$  is the coupling between the two diabatic potentials, and the diagonal elements  $H_j$  of the total Hamiltonian are given as

$$H_j = -\frac{1}{2M} \nabla^2 + V_j(Q, R) \quad (4)$$

where  $V_j(Q, R)$  is the potential energy as a function of the configurational coordinates  $Q$  and  $R$  and  $-1/2M \cdot \nabla^2$  is the nuclear kinetic energy.

For simplicity, we chose harmonic potentials in all of the following examples, although the methods used are not restricted by the functional form of the potentials. The displacement of the minimum of one electronic state from the other, from that of the ground state,  $\Delta Q$ , is abbreviated as  $\Delta$  in this paper. The potentials are given by:

$$V_j(Q, R) = \frac{1}{2} k_j (Q \pm \Delta Q_j)^2 + \frac{1}{2} k_j' (R - \Delta R_j)^2 + E_j \quad (5)$$

with  $\Delta Q_j$  and  $\Delta R_j$  the positions of the potential minima along  $Q$  (asymmetric coordinate) and  $R$  (symmetric coordinate).  $k_j = 4\pi^2 M (h \omega_j)^2$  and  $k_j' = 4\pi^2 M (h \omega_j')^2$  are the force constants along coordinates  $Q$  and  $R$ , respectively, and  $E_j$  is the energy of the potential minimum for state  $j$ . These uncoupled potentials are shown in Figure 2.

The equation of the autocorrelation function for a coupled two excited electronic state system can be written as<sup>23</sup>

$$\langle \phi | \phi(t) \rangle = \sum_{i=1}^2 \sum_{j=1}^2 (\bar{\mu}_j \cdot \bar{e}_1) (\bar{\mu}_i \cdot \bar{e}_1) \langle e_i | \langle \chi_0 | C_i^* e^{-iHt} C_j | \chi_0 \rangle | e_j \rangle \quad (6)$$

where  $|\chi_0\rangle$  is the initial wave function from the ground electronic state and  $|e_i\rangle$  with  $i = 1, 2$  is the two excited electronic states.  $\mu_i$  and  $C_i$  are the transition dipole moment direction and magnitude, respectively, and  $e_1$  is the polarization vector of light.

For the M–B–M type systems studied in this paper, the transition dipole moment magnitudes are equal by symmetry but their direction depends on the geometry of the molecule. The relative orientation between the dipoles is defined by the angle  $\beta$ . When this molecule–fixed dipole orientation is averaged over all angles to account for the usual case of randomly oriented molecules with respect to the polarization vector of light,  $e_1$ , the average

$$\langle (\bar{\mu}_j \cdot \bar{e}_1) (\bar{\mu}_i \cdot \bar{e}_1) \rangle = \begin{cases} \frac{1}{3} & \text{when } i = j \\ \frac{1}{3} \cos\beta & \text{when } i \neq j \end{cases} \quad (7)$$

gives rise to the following form of the autocorrelation function:

$$\langle \phi | \phi(t) \rangle = \frac{1}{3} ( \langle \phi_1 | \phi_1(t) \rangle + \cos\beta \langle \phi_1 | \phi_2(t) \rangle + \cos\beta \langle \phi_2 | \phi_1(t) \rangle + \langle \phi_2 | \phi_2(t) \rangle ) \quad (8)$$

**Raman Spectroscopy.** Raman intensity is governed by the following equation:

$$I_R(\omega) = \omega_1 \omega_s^3 |\alpha|^2 \quad (9)$$

where the polarizability term  $\alpha$  for the two state system is given by

$$\alpha(\omega) = \int_0^\infty e^{i\omega t - \Gamma t} \sum_i^2 \sum_j^2 (\bar{\mu}_i \cdot \bar{e}_s) (\bar{\mu}_j \cdot \bar{e}_1) \langle \phi_j | \phi(t) \rangle_{ij} dt \quad (10)$$

where  $\bar{e}_s$  is the polarization vector of scattered light and  $i$  and  $j$  are to two excited states. When the angle average of  $|\alpha|^2$  over all orientations is included, eq 9 becomes

$$I_R = \omega_1 \omega_s^3 \left( \sum_i^2 \sum_j^2 \sum_k^2 \sum_l^2 \langle G_{ij}^* G_{kl} \rangle \alpha_{ij}^* \alpha_{kl} \right) \quad (11)$$

where  $G_{ij}$  is

$$G_{ij} = (\bar{\mu}_i \cdot \bar{e}_s) (\bar{\mu}_j \cdot \bar{e}_1) \quad (12)$$

and the brackets  $\langle \rangle$  denote the average over all orientations of space. The polarization vector of the laser is chosen again to be in the  $z$ -direction and  $e_s$  can be either  $x$ -,  $y$ - or  $z$ -polarized. Equation 11 describes the angle-averaged Raman intensity for one polarization of the scattered light. The total Raman intensity (all polarizations of scattered light) is the sum over all three scattered light polarizations of the  $I_R$  terms. The equation for the angle-averaged total resonance Raman intensity in terms of the molecule-fixed  $\beta$  angle is

$$\frac{4\pi^2}{3} \left[ 2 \sum_i^2 \sum_j^2 |\alpha_{ij}|^2 + (1 + \cos 2\beta) (\alpha_{11}^* \alpha_{22} + \alpha_{12}^* \alpha_{21} + \alpha_{21}^* \alpha_{12} + \alpha_{22}^* \alpha_{11}) + 2 \cos\beta (\alpha_{11}^* \alpha_{12} + \alpha_{11}^* \alpha_{21} + \alpha_{12}^* \alpha_{11} + \alpha_{21}^* \alpha_{11} + \alpha_{22}^* \alpha_{12} + \alpha_{22}^* \alpha_{21} + \alpha_{12}^* \alpha_{22} + \alpha_{21}^* \alpha_{22}) \right] \quad (13)$$

In the case of the ESMV system studied in this paper,  $\alpha_{11} = \alpha_{22}$ ,  $\alpha_{12} = \alpha_{21}$ , and eq 13 simplifies to

$$8\pi^2 \left[ \left( 1 + \frac{1}{3} \cos 2\beta \right) (|\alpha_{11}|^2 + |\alpha_{12}|^2) + \frac{4}{3} \cos\beta (\alpha_{11}^* \alpha_{12} + \alpha_{12}^* \alpha_{11}) \right] \quad (14)$$

## Results

The solution and solid state absorption spectra of  $\mathbf{1}^+$  are shown in Figure 1. The lowest energy absorption band of  $\mathbf{1}^+$  consists of two components with peak maxima at 15200 and 22000  $\text{cm}^{-1}$  in solution and at 14900 and 21600  $\text{cm}^{-1}$  in the solid state. The fwhm of the lower energy component for the solution (solid state) spectrum is 5500  $\text{cm}^{-1}$  (6500  $\text{cm}^{-1}$ ), and the fwhm of the higher energy component is 3300  $\text{cm}^{-1}$  ( $\sim$ 4300  $\text{cm}^{-1}$ ). The absorption spectrum of  $\mathbf{2}^+$  is also presented in Figure 1 and consists of a single peak at 19600  $\text{cm}^{-1}$  with a fwhm of 6100  $\text{cm}^{-1}$ .

Resonance Raman spectra obtained using 676 and 476 nm excitation are shown in Figure 3. The observed frequencies (in wavenumbers) and the integrated intensities for those modes (normalized to the intensity of the 1055  $\text{cm}^{-1}$  nitrate peak of the standard) are summarized in Table 1. The bands listed have an intensity of at least 10% of that of the most intense band at 1264  $\text{cm}^{-1}$  and have been corrected for self-absorption. The

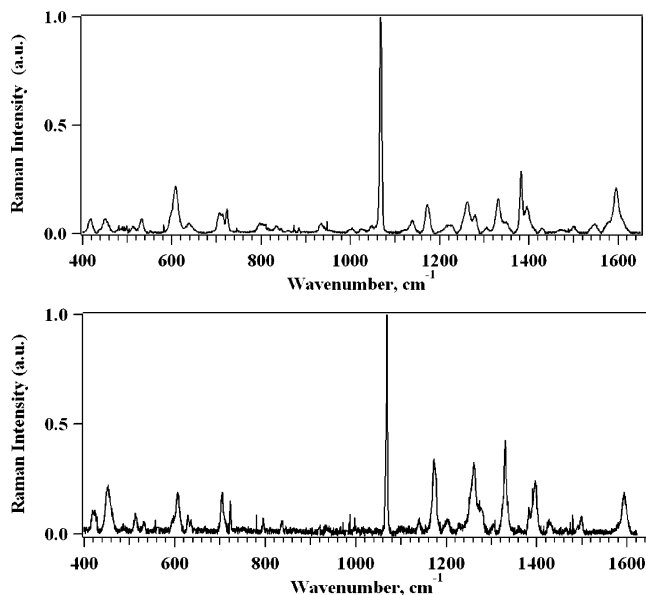


**Figure 3.** Resonance Raman spectra of  $1^+$  obtained using 476 (top panel) and 676 nm (bottom panel) excitation.

calculated frequencies for the vibrational modes assigned to the experimental resonance Raman bands also appear in Table 1.

## Discussion

**1. ESMV Model.** The ESMV behavior of  $1^+$  ( $C_2$  symmetry) is modeled by two interacting 2D harmonic potential energy surfaces in the excited state as shown in Figure 2. While these surfaces are portrayed along both a symmetric and an asymmetric coordinate, the physical meaning of ESMV is best explained by considering the excited state surfaces along only the asymmetric coordinate. The symmetric coordinate in the ESMV model is introduced in the next section. A single harmonic surface with its minimum at zero along the asymmetric vibrational coordinate represents the ground state with the charge localized on the nitrogens. Electronic charge transfer transitions from each of the phenyl groups to the hydrazine unit send the +1 charge to one phenyl group or the other. Symmetry requires that these transitions be equal in energy and occur with equal probability. In the model, these energetically equal transitions give rise to two diabatic surfaces in the excited state that are degenerate at  $Q = 0$ , each representing the system with the charge localized on one of the phenyl groups. The excited state diabatals are displaced from the ground state surface such that the Franck–Condon region of each diabatic has a nonzero slope that is equal in magnitude and opposite in sign. The diabatic surfaces couple, creating two new nondegenerate adiabatic surfaces with an energy splitting of  $2H_{\text{eff}}$  at  $Q = 0$  between the lower and the higher energy adiabatic surfaces.

**2a. Spectroscopic Consequences: Absorption Spectroscopy.** Both components of the absorption spectrum of  $1^+$  shown in Figure 1 are assigned to the transition to the mixed valence excited state. The effects of excited state coupling are revealed through three different properties of the absorption spectrum: the energy splitting, the relative intensities, and the relative bandwidths of the two bands.

*Energy Splitting.* The two absorption band components at 15200 and 22000  $\text{cm}^{-1}$  correspond to the transition to the lower and upper adiabatic surface, respectively. The difference in energy between the two peak maxima, therefore, is directly related to the magnitude of coupling between the diabatic surfaces in the excited state. If the coupling had been zero, a single peak would have been observed in the absorption spectrum because the transition to one diabatic surface produces the same spectrum as a transition to the other. This “zero coupling” case is illustrated analogously by the absorption spectrum of the monophenyl hydrazine species,  $2^+$ , also shown in Figure 1. Because only one phenyl–hydrazine transition is possible, its excited state can be modeled by one displaced harmonic surface. Consequently, the lowest energy absorption band of this molecule consists of a single peak at 19600  $\text{cm}^{-1}$  that is between the energies of the two peaks of  $1^+$ .

*Relative Intensities.* The intensity ratio of the two peaks is dictated by three factors: the magnitude of the effective coupling,  $H_{\text{eff}}$ , the sign of  $H_{\text{eff}}$ , and the spatial orientation between the transition dipole moments. The sign of the coupling is important because it determines the identities of the upper and lower adiabatic surfaces. The sign of the coupling was addressed in the study of the diphenyl cation compound using a neighboring orbital analysis<sup>2</sup> based on the work of Hoffmann et al.<sup>46,47</sup>  $H_{\text{eff}}$  for that molecule was determined to be positive. While the addition of the para-substituted methoxy groups alters the magnitude of  $H_{\text{eff}}$  in  $1^+$ , as indicated by the different energy splitting of the absorption bands of the two species, it does not change its sign so the sign of the effective coupling for  $1^+$  is also positive.

The spatial orientation of the transition dipole moments also dictates the relative intensity ratio of the two components of the absorption band. The relative orientation between the dipoles is defined by the angle  $\beta$ . To account for the case of randomly oriented molecules in solution with respect to the polarization vector of light,  $\bar{e}_1$ , the molecule-fixed dipole angle must be averaged over all angles of orientation. The averaging of the cross-terms,  $\langle (\bar{\mu}_j \cdot \bar{e}_1) (\bar{\mu}_i \cdot \bar{e}_1) \rangle$  in eq 6 leads to the  $1/3 \cos \beta$  term in the autocorrelation function in eq 8. The Fourier transform of this correlation function gives the absorption spectrum where the intensity ratio of the two components is governed by the angle  $\beta$ . The selection rules associated with the two extremes of dipole moment orientation, “parallel”,  $\mu_1 = \mu_2$  and “antiparallel”,  $\mu_1 = -\mu_2$ , were derived in our recent

**TABLE 1: Resonance Raman Frequencies and Intensities for  $1^+$**

frequency ( $\text{cm}^{-1}$ )	$I_k/I_k'$ 676 nm	$\Delta_{676}$	$I_k/I_k'$ 476 nm	$\Delta_{476}$	$(I_k/I_k')_{676}/$ $(I_k/I_k')_{476}$	calcd frequency ( $\text{cm}^{-1}$ )	assignment
418	0.527	1.71	0.150	0.787	3.5	426	Ph. ring def.
450	1.38	2.56	0.202	0.848	6.8	486	C–N–N–C twist
532	0.240	0.904	0.127	0.569	1.9	542	C–N–N–C twist
608	0.980	1.60	0.768	1.22	1.3	611	C–N–N–C twist
707	0.639	1.11	0.201	0.538	3.2	715	C–N–N–C twist
1140	0.228	0.412	0.127	0.265	1.8	1165	N–N str.
1174	1.37	0.977	0.207	0.329	6.6	1204	C–N str. with Ph. C–H wag
1264	1.85	1.06	0.359	0.402	5.2	1327	Ph. ring def. with C=O str.
1333	1.37	0.863	0.301	0.349	4.6	1381	Ph. ring def. with N–N str.
1397	0.954	0.686	0.213	0.280	4.5	1432	N–N str.
1596	0.904	0.585	0.516	0.382	1.8	1661	Ph. C–C str.

study of the diphenyl compound.<sup>2</sup> The result was that for parallel dipoles and positive  $H_{\text{eff}}$ , only the transition to the upper adiabatic surface is fully allowed. For antiparallel dipoles, only the transition to the lower adiabatic is fully allowed. When  $\beta = 0^\circ$ , eq 8 is equal to the correlation function that results from the  $\mu_1 = \mu_2$  parallel dipole orientation because it becomes the straight sum

$$\frac{1}{3} \sum_i^2 \sum_j^2 \langle \phi_i | \phi_j(t) \rangle$$

When  $\beta = 180^\circ$ , eq 8 becomes

$$\langle \phi | \phi(t) \rangle = \frac{1}{3} (\langle \phi_1 | \phi_1(t) \rangle - \langle \phi_1 | \phi_2(t) \rangle - \langle \phi_2 | \phi_1(t) \rangle + \langle \phi_2 | \phi_2(t) \rangle) \quad (15)$$

which is the same form of the correlation function that results for  $\mu_1 = -\mu_2$ , i.e., antiparallel dipoles. For systems with  $\beta$  between 0 and  $180^\circ$ , both transitions are allowed and the intensities of the two absorption bands are governed by the  $\cos \beta$  weighting of the cross-terms in eq 8. The relative intensities can also be interpreted as being weighted by the magnitude of the parallel and antiparallel vector transition dipole moment components. The total spectrum then results from the sum of the spectra resulting from parallel and antiparallel dipoles weighted by the appropriate magnitude of their vector projections. The ratio of the oscillator strengths of the parallel and antiparallel components,  $f_p$  and  $f_a$ , is given by<sup>2</sup>

$$\frac{f_a}{f_p} = \frac{\mu_a^2}{\mu_p^2} = \left( \tan \frac{\beta}{2} \right)^2 \quad (16)$$

**Relative Bandwidths.** The bandwidths of the two absorption band components are significantly different. In fact, the fwhm of the lower energy component is over one and a half times wider than that of the higher energy component. The key factor in absorption bandwidth is the slope of the excited state surfaces in the Franck–Condon region. The slope is determined by both the frequency and the displacement of the potential surface along each normal coordinate. For ground state mixed valence systems with large coupling (class III), both asymmetric and symmetric coordinates must be included to accommodate absorption spectrum bandwidths.<sup>9,48,49</sup> In systems such as this with large coupling, both of the excited state adiabatic surfaces possess single minima, which are undisplaced relative to the ground state surface along the asymmetric coordinate (i.e., the slope in the F–C region along the asymmetric coordinate is zero). Spectra resulting from the transition to these one-dimensional ESMV surfaces possess two components with similarly narrow bandwidths due to the lack of vibronic progressions. As a result, the asymmetric coordinate alone cannot be used to explain the large difference in bandwidth.

We interpret the absorption bandwidth for both components to be caused predominantly by displacements of the excited state surfaces along symmetric coordinates. In the ESMV model, the diabatic surfaces are represented along each symmetric coordinate by two nested harmonic potentials with equal displacement as shown in Figure 2. When coupling is included, the resulting adiabatic surfaces have a nonzero slope in the F–C region. If coupling is constant, the degeneracy is removed and the adiabatic surfaces are separated in energy by  $2H_{\text{eff}}$  at every point along the coordinate. Consequently, the adiabatic surfaces

retain the same displacement along the symmetric coordinate as the diabatic surfaces. This results in two absorption band components of equal width. Adding a linear coordinate dependence to the coupling gives rise to different displacements of the adiabatic surfaces as shown in Figure 2. The spectroscopic consequence of this coordinate-dependent coupling is that the absorption band associated with the transition to the more displaced adiabatic will be broader than that associated with the less displaced one. In the absorption spectrum of  $\mathbf{1}^+$ , the wider bandwidth of the lower energy component indicates that the displacement along the symmetric coordinates is larger overall for the lower energy adiabatic surface than for the higher energy one. In our model, this translates to positive coordinate-dependent coupling. The physical origin and meaning of the coordinate dependence of the coupling will be discussed in section 5.

**2b. Calculated Absorption Spectrum.** To calculate a fit to the absorption spectrum, appropriate parameters must be chosen to define the ground and excited state surfaces. First, the frequency must be chosen for the asymmetric mode of the ESMV surfaces. The asymmetric modes of  $\mathbf{1}^+$  are not expected to undergo significant enhancement in the resonance Raman spectrum. Therefore, only frequencies of modes that are exclusively IR-active were considered in defining the ground and excited state surfaces along the asymmetric coordinate. The Phenyl-to-Hy transition is expected to involve (phenyl)C–N stretching modes as well as CNNC twist modes. The resonance Raman data in Table 1, which will be discussed in detail in section 4, show that the symmetric modes that undergo the biggest distortions are the low frequency CNNC twist modes. The asymmetric CNNC twist modes are expected to have similar distortions and occur in the same frequency region as their symmetric mode counterparts, which occur around  $500 \text{ cm}^{-1}$ . The experimental IR spectrum shows several unresolved peaks in this frequency region. The molecular orbital calculation for this molecule yields an asymmetric normal mode at  $487 \text{ cm}^{-1}$  involving significant change in the CNNC twist angle. We chose this frequency to define the ground state harmonic potential surface along the asymmetric coordinate. Coupling of the excited state surfaces along the asymmetric coordinate is constant, and the optimal  $H_{\text{eff}}$  is  $3350 \text{ cm}^{-1}$ . Changing this value by more than  $\pm 100 \text{ cm}^{-1}$  results in significantly poorer calculated fits to the experimental spectra.

The constant component of  $H_{\text{eff}}$  is determined from experiment (i.e., from the splitting in the absorption spectrum) whereas  $\Delta$  is not. Because the asymmetric modes in this molecule are not Raman active and resonance enhancement is extremely small, we cannot use resonance Raman intensity to obtain a value for the displacement. We make the assumption that the  $\Delta$  values for both the symmetric and the asymmetric modes are comparable and chose a value of 1.5, which is comparable to the  $\Delta$  values of similar symmetric modes.

The symmetric modes in the molecule are responsible for the bandwidths of the absorption spectrum. As explained in the previous section, the difference in bandwidth between the two absorption spectrum components results from the coordinate dependence of the coupling along all of the symmetric coordinates. There are at least eight symmetric modes that are significantly resonantly enhanced in this molecule, each contributing its own coordinate dependence to the excited state coupling. The multidimensional calculation required to accommodate all of these modes and the asymmetric mode (minimum of nine dimensions) is beyond our computational means. Therefore, the absorption spectrum calculation in this study is

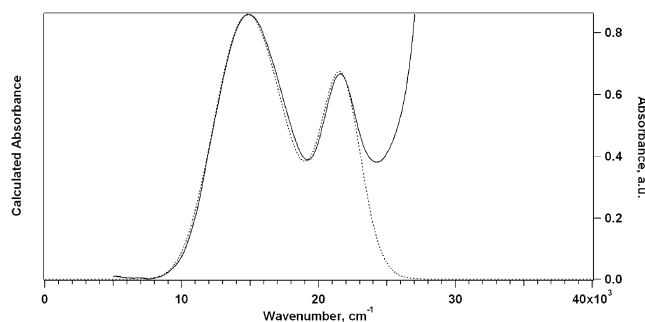


**Figure 4.** Calculated fit (dotted line) to experimental solid state absorption spectrum (solid).

limited to two dimensions: one asymmetric coordinate and one symmetric coordinate. The symmetric coordinate in this model represents all of the symmetric modes in a molecule that significantly contribute to the absorption bandwidths. By subsuming all of the symmetric coordinates into one, the difference in bandwidth must then be achieved with one coordinate-dependent contribution to the coupling. This coordinate-dependent coupling represents the combination of coordinate dependencies from all of the individual symmetric modes. Because the bandwidths of the two components of the absorption spectrum result from the composite of all of the symmetric modes coordinate dependencies, the representative single symmetric coordinate must necessarily have a large coordinate dependence. This is required in order to achieve the same difference in bandwidth as produced by the collaboration of all of the contributing symmetric modes. The symmetric mode assigned as a symmetric C–N stretch with a frequency of  $1174\text{ cm}^{-1}$  is chosen from Table 1 as the representative symmetric mode because, with its large displacement and frequency, it is expected to be one of the dominating symmetric modes affecting the spectrum. The nested diabatic potentials along this coordinate have a displacement of 1.56. To produce the appropriate bandwidths, a coordinate dependence of  $1248\text{ cm}^{-1}$  is included in the excited state coupling.

The absorption spectrum calculated using the 2D surfaces just described is shown in Figure 4. As the figure reveals, the two components of the total calculated absorption spectrum occur at the appropriate energies and have the necessary intensity ratio and bandwidths to fit the experimental spectrum. The combination of the symmetric and asymmetric modes is required to produce the overall bandwidth and band shape. The damping factor,  $\Gamma$ , was  $970\text{ cm}^{-1}$  in this calculation. On the basis of the ground state geometry where the nitrogens have approximately  $sp^2$  hybridization, the angle between the two transition dipole moments,  $\beta$ , was expected to be about  $120^\circ$ . The best fit to the absorption spectrum was calculated using  $\beta = 125^\circ$  in eq 8.

**3. Spectroscopic Consequences: Resonance Raman Spectroscopy.** Resonance Raman spectroscopy is used to determine the frequencies and relative displacements (determined from the intensities) of the excited state along the symmetric coordinates. Raman spectra of  $1^+$  were obtained in resonance with both the high and the low energy components of its absorption band and are shown in Figure 3 and summarized in Table 1. We expected the ratios of these two sets of resonance Raman intensities to match the relative intensities of the two absorption band components. Instead, the intensity ratios of almost all modes in the Raman spectrum obtained using  $676\text{ nm}$  vs  $476\text{ nm}$  excitation are significantly larger than the intensity ratio of the two components of the absorption spectrum at these wavelengths. This ratio for some modes is over five times bigger than that of the absorption band intensities.

This apparent discrepancy is a result of the coupling and involves two factors: the averaging of the dipole moment orientation over all orientations as it applies to resonance Raman spectroscopy and the effect of coordinate-dependent coupling on the resonance Raman intensity. These factors are discussed below.

*Orientational Averaging of Transition Dipoles.* As was the case for the absorption spectrum of an ESMV system, the orientation of the transition dipole moments dictates the relative intensity ratio of the two components of the resonance Raman profile. One reason that the relative intensities of the resonance Raman profiles do not match those of the absorption spectrum is that the angle averaging of the molecule-fixed dipole moment orientation is different for the two processes. The angle averaging associated with the absorption process, which results in the cosine  $\beta$  weighted sum in the expression for the correlation functions (eq 7), allows the total absorption spectrum to be calculated as the weighted sum of the parallel and antiparallel components. This simple sum cannot be used to generate the angle-averaged resonance Raman profiles because resonance Raman intensity is dictated by the polarizability tensor,  $\alpha$ , as shown in eq 9, and the orientational averaging is included after squaring this term. The result is a much more complicated expression, which cannot be separated into parallel and antiparallel components as was possible for the absorption averaging. Another important difference between the two types of spectroscopy that affects the dipole orientation averaging is that absorption spectroscopy is a one-photon process whereas Raman involves two photons. Consequently, for the absorption process, the averaging only applies to the orientation of the dipoles relative to the polarization vector of the incident light,  $\vec{e}_i$ , whereas for Raman, the averaging is carried out with respect to both the vector polarization of the incident light and the scattered light. While in the case of laser excitation, only one  $\vec{e}_i$  direction is needed (defined as  $z$ -polarization in this study), the scattered light from the randomly oriented sample can occur in the  $x$ -,  $y$ -, and  $z$ -polarizations and so all three polarizations must be included in the averaging.

The consequence of angle averaging in these two spectroscopic processes is that the resonance Raman intensity ratio of the low to high energy component can be very different than the absorption spectrum's low to high energy component ratio depending on the dipole moment orientation. For the  $\beta$  angle in  $1^+$ , which is determined to be  $125^\circ$  based on the calculated fit to the absorption spectrum, the ratio calculated is significantly larger in the resonance Raman profile than in the absorption spectrum. This effect of angle averaging on resonance Raman intensities is illustrated in Figure 5 where the resonance Raman intensities calculated using constant coupling,  $H_{\text{eff}} = 3350\text{ cm}^{-1}$  and  $\beta = 125^\circ$  are compared with the experimental absorption spectrum of  $1^+$ . The symmetric mode chosen for this example has a frequency of  $450\text{ cm}^{-1}$  and a displacement of the nested diabatic potentials along this coordinate of 1.7. As discussed in section 2, constant coupling yields adiabatic surfaces having the same displacement as the nested diabatic surfaces along the coordinate. Figure 5 shows that the resonance Raman intensity ratio of the low to high energy component of the Raman profile calculated with constant coupling is significantly smaller than the value of the absorption spectrum ratio. This calculation, therefore, shows that the averaging of the transition dipole moment orientation is at least in part responsible for the observed intensity ratio difference between the absorption and the resonance Raman spectra.

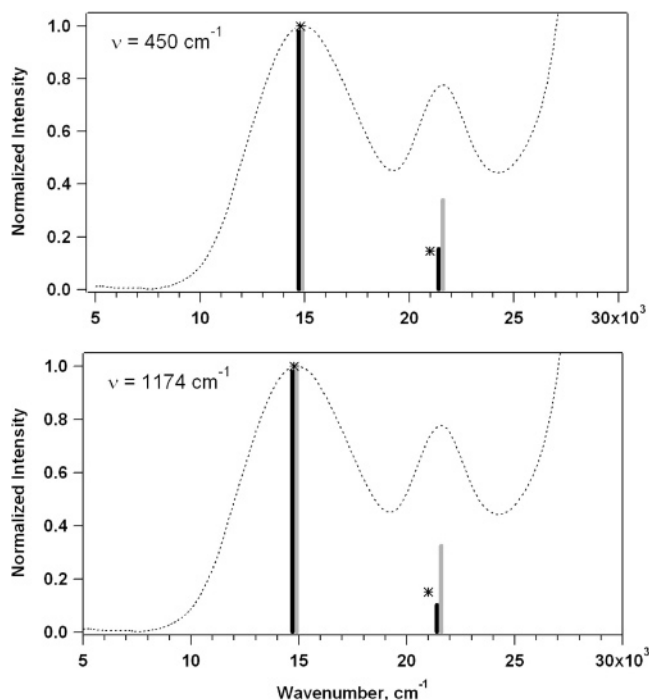


**Figure 5.** Resonance Raman intensity calculated with  $\beta = 125^\circ$  and constant (gray bar) and coordinate-dependent (black bar) coupling, as compared to experimental absorption (dashed line) and experimental resonance Raman intensities (\*).

*Coordinate-Dependent Coupling.* The experimental resonance Raman intensity ratio for the  $450\text{ cm}^{-1}$  mode example above is still much larger than that calculated after orientational averaging of the  $\beta$ -angle is included. This difference is explained by the coordinate dependence of the coupling. In the adiabatic limit, the interpretation of the different resonance Raman intensity ratios leads to two different sets of displacements along the symmetric coordinates, one associated with the upper adiabatic excited state surface and the other associated with the lower adiabatic excited state surface. If the orientation of the transition dipoles were the only factor affecting the resonance Raman intensities, then for each of the resonantly enhanced modes, the ratio of the two components of the profile would be the same. This is not the case for  $\mathbf{1}^+$  as indicated by the large range of resonance Raman intensity ratios listed in Table 1. These different intensity ratios can be explained by the coordinate dependence of the coupling. As discussed in the absorption spectroscopy section, when the excited state coupling includes a coordinate dependence, one adiabatic surface becomes less displaced and the other adiabatic becomes more displaced than the original diabatic surfaces along the symmetric coordinate. Consequently, when the wave packet propagates on the two coupled surfaces, it encounters a slope that is bigger for one adiabatic than the other. When the damping factor is large enough that the overlap at short times dominates, as is expected for this study, the wave packet propagation on the more displaced adiabatic will yield larger Raman intensities because overlap develops faster in time.

Resonance Raman intensity ratios that are significantly larger than those predicted after orientational averaging is included can be interpreted as having a large coordinate dependence. To illustrate the effect of coordinate-dependent coupling on the resonance Raman intensity, we return to the  $450\text{ cm}^{-1}$  symmetric mode example. The same parameters as previously described are used for this calculation. The initial displacement of the nested diabatic potentials along this coordinate is

estimated as the average of the displacements derived from the two resonance Raman spectra obtained with 476 and 676 nm excitation. These displacements, presented in Table 1, are obtained using the standard method of interpreting resonance Raman intensity.<sup>24</sup> When a linear coordinate dependence is added to the coupling ( $3400 + 384 \cdot Q\text{ cm}^{-1}$ , where  $Q$  is the  $450\text{ cm}^{-1}$  symmetric coordinate), the resulting upper and lower adiabatic surfaces have displacements that match  $\Delta_{476}$  (upper adiabatic) and  $\Delta_{676}$  (lower adiabatic) of Table 1 for this mode. The ratio of resonance Raman intensities calculated using the coordinate-dependent coupling matches the experimental intensity ratio as shown in Figure 5. The value of  $\Gamma$  in both calculations is  $1000\text{ cm}^{-1}$ . The intensity ratio for the profile calculated with constant coupling is the same regardless of the magnitude of the damping factor, whereas the intensity ratio for the profile calculated with coordinate-dependent component added to the coupling is quite sensitive to the value of  $\Gamma$ .<sup>50</sup> The damping factor is not a known quantity and is difficult to measure experimentally, since it represents many dephasing processes including solvent interactions and other vibrational modes. For this reason, we have a limited quantitative understanding of the true intensity ratio that results from the coordinate dependence of the coupling. However, the trend holds that modes with Raman intensity ratios that significantly deviate from those predicted for the system with a given transition dipole orientation and constant coupling have a large coordinate-dependent contribution to the coupling. The symmetric mode examined in this section is the best example to illustrate the effect of the coordinate dependence of the coupling because it is the most highly distorted mode with largest resonance Raman intensity ratio. Given the trend established by analyzing this mode, the origin of the coordinate dependence of the coupling for this and other important symmetric modes will be explained in section 5 after the vibrational mode assignments are discussed in the next section.

**4. Vibrational Mode Assignments.** The structural changes that  $\mathbf{1}^+$  experiences in the mixed valence excited state are explained by the resonance Raman data and vibrational assignments. Vibrational assignments are made by comparing the calculated vibrational modes with the observed resonance Raman frequencies as presented in Table 1. Resonance Raman shows enhancement of many low frequency modes (below  $800\text{ cm}^{-1}$ ) that involve significant C–N–N–C twist angle changes. Of these low frequency modes, the ones at  $450$  and  $608\text{ cm}^{-1}$  show the greatest resonance enhancement. The lowest frequency mode appears at  $418\text{ cm}^{-1}$  and is assigned as an out-of-plane phenyl ring deformation. Higher frequency modes involving C–N and/or N–N bond length changes also show significant displacement. The mode at  $1174\text{ cm}^{-1}$  is assigned to a symmetric C–N stretching mode, and the modes at  $1140$  and  $1397\text{ cm}^{-1}$  are assigned to symmetric modes with significant N–N stretching character. Phenyl ring deformation modes that include symmetric C–O and N–N stretching occur at  $1264$  and  $1333\text{ cm}^{-1}$ , respectively. The highest energy mode at  $1596\text{ cm}^{-1}$  involves phenyl ring CC stretching.

These structural changes are consistent with those expected for the phenyl to hydrazine charge transfer. On the basis of the MO calculations for  $\mathbf{1}^+$ , the higher energy electronic transition occurs from a molecular orbital that is bonding across the two C–N bonds to an orbital that is antibonding across C–N. Consequently, significant C–N bond length changes are expected to occur upon excitation. Similarly, the lower energy electronic transition occurs from a molecular orbital that is bonding across the bridge to an orbital that is antibonding across

the bridge. Therefore, a change in the N–N bond length is expected in the excited state. Because this electronic transition also promotes a change in nitrogen hybridization from  $sp^2$  to  $sp^3$ , modes involving the C–N–N–C twist angle change are expected to be important.

**5. Origin of the Coordinate-Dependent Coupling.** The coupling is coordinate-dependent when the interaction between the two charge bearing units is altered by the changes in bond length and bond angle associated with a normal vibrational mode. In this study, the coupling between the two charge-bearing phenyl units is mediated by the  $\pi$ -orbital system through the hydrazine bridge. Therefore, this through bond coupling is expected to be sensitive to normal modes of vibration that change the  $\pi$ -orbital overlaps of the MOs involved in the ESMV transition. Because some types of vibrations will induce a greater change in orbital overlap than others, we expect the coupling to have a coordinate dependence that is larger along some symmetric coordinates than along others. In the previous section, we showed that a large coordinate dependence of the coupling along the  $450\text{ cm}^{-1}$  symmetric CNNC twist mode produced a resonance Raman intensity ratio that could accommodate the experimental ratio. Because the overlap of the bridge with phenyl  $\pi$ -systems will be perturbed by the  $sp^2$  to  $sp^3$  twist, a large coordinate-dependent contribution to the coupling is expected for this type of mode.

C–N stretching modes are also expected to have a large effect on the coupling. One example is the mode assigned as a C–N stretch at  $1174\text{ cm}^{-1}$ . The magnitude of coupling is expected to be sensitive to this and other C–N stretching modes because changing the C–N bond lengths will change the  $\pi$ -overlap between the hydrazine and the phenyl groups. Figure 5 (bottom panel) shows that the experimental resonance Raman intensity ratio of the low to high energy components is much larger than the absorption band ratio and still larger than the resonance Raman intensity ratio calculated for this mode with  $3350\text{ cm}^{-1}$  constant coupling. A linear coordinate dependence of  $382\text{ cm}^{-1}$  included with the constant component of the coupling effectively displaces the upper and lower adiabatic surfaces to the values of  $\Delta_{476}$  (upper adiabatic) and  $\Delta_{676}$  (lower adiabatic) listed in Table 1 for this mode. Once this coordinate dependence is included, the calculated intensity ratio matches the experimental ratio, as shown in Figure 5.

On the other hand, the coupling will not be as influenced by vibration along normal coordinates that do not change the orbital overlap. For example, the mode observed at  $1596\text{ cm}^{-1}$  and calculated at  $1661\text{ cm}^{-1}$ , assigned as a CC phenyl stretch, predominantly involves changes in the C<sub>2</sub>–C<sub>3</sub> and C<sub>5</sub>–C<sub>6</sub> bonds of the phenyl groups. The coupling is not expected to be significantly affected by changing these bond lengths because the relevant MOs (i.e., the MOs involved in the through bond coupling) have a node across these CC bonds of the phenyl. Because there is little orbital overlap to begin with, changing these bond lengths has little effect on the magnitude of coupling. The experimental resonance Raman intensity ratio for this mode is consistent with this prediction. While the ratio is larger than that of the absorption spectrum as a result of the averaging of the dipole moment orientation, it is not nearly as large as would be predicted with significant coordinate-dependent coupling. A similar analysis can be used to explain the resonance Raman intensity ratio of the phenyl ring deformation vibrational mode observed at  $418\text{ cm}^{-1}$  and calculated at  $426\text{ cm}^{-1}$ . The motion of this mode is almost completely localized on the phenyl groups. Consequently, there is little change to the  $\pi$ -interaction with the bridge upon vibration and the coupling is not expected

to be significantly altered. This prediction is supported by the experimental resonance Raman intensity ratio, which is closer to that predicted with constant coupling only.

The experimental resonance Raman intensity ratios in Table 1 can be explained by a combination of the orientational averaging of the transition dipole moments and the coordinate dependence of the coupling. Using a simple model that includes a linearly dependent coordinate dependence, we explain the observed resonance Raman intensities and establish the trend that significant deviation of the intensity ratio from that predicted using constant coupling is a result of coordinate-dependent coupling. In the two specific modes analyzed in this section ( $450$  and  $1174\text{ cm}^{-1}$ ), the larger than predicted ratio was accommodated by adding a coordinate dependence to the coupling. The origin of the coordinate dependence is explained by the expected orbital overlap change for each vibrational motion.

## Summary

Two important factors influence the observed features of the absorption and resonance Raman spectra for the di-*p*-anisyl hydrazine cation,  $\mathbf{1}^+$ : the effective excited state coupling and transition dipole moment orientation. The magnitude of the effective excited state coupling dictates the energy splitting between the two components of the absorption band assigned to the ESMV transition. The intensity ratio of the absorption band components is attributed to a combination of the sign of the coupling, which is positive in the case of  $\mathbf{1}^+$ , and the molecule-fixed transition dipole moment orientation, which must be averaged over all orientations to account for the random orientation of the molecules in the sample. The difference in width between the two components arises because the coordinate dependence of the coupling effectively places the adiabatic surfaces at different displacements along the normal coordinate from the ground state equilibrium geometry. We fit the experimental absorption spectrum using a wave packet propagation method with 2D two-state potential energy surfaces (one asymmetric and one symmetric coordinate). The symmetric coordinate used in the calculation represented all of the symmetric modes in the molecule with significant displacement from the ground state geometry. The combined effect of the coordinate-dependent contributions to the coupling of each individual mode was represented by the one coordinate dependence of the coupling along this representative symmetric coordinate.

The averaging of the transition dipole moment orientation is not the same for absorption and resonance Raman spectroscopy. Consequently, the resonance Raman profile is not expected to follow the absorption band contour. For the  $125^\circ$  orientation angle of the transition dipole moments of  $\mathbf{1}^+$ , the intensity ratio of the low to high energy component of the Raman profile is predicted to be greater than that of the absorption band in agreement with the experiment. The resonance Raman intensity ratios will vary from mode to mode depending on the coordinate-dependent contribution to the coupling. The observed resonance Raman intensities support these theoretical predictions. The majority of the modes exhibit an intensity ratio that is considerably larger than that observed in the absorption spectrum. The significant deviations from the ratio theoretically predicted using constant coupling are explained by the coordinate-dependent component of the coupling. Given the vibrational assignments, the origin of the coordinate-dependent coupling is discussed for the different types of symmetric modes that are resonantly enhanced.

**Acknowledgment.** We thank the NSF for Grants CHE-0240197 (S.F.N.) and CHE0206857 (J.I.Z.) for partial financial support of this work and for NSF Grant CHE0091916 and for gifts from the Intel Corp. for support of the departmental computers used in this work. This work was also made possible by a UCLA dissertation year fellowship to J.V.L.

## References and Notes

- (1) Lockard, J. V.; Zink, J. I.; Konradsson, A. E.; Weaver, M. N.; Nelsen, S. F. *J. Am. Chem. Soc.* **2003**, *125*, 13471.
- (2) Lockard, J. V.; Zink, J. I.; Trieber, D. A.; Konradsson, A. E.; Weaver, M. N.; Nelsen, S. F. *J. Phys. Chem. A* **2005**, *109*, 1205.
- (3) Hush, N. S. *Prog. Inorg. Chem.* **1967**, *8*, 391–444.
- (4) Hush, N. S. *Coord. Chem. Rev.* **1985**, *64*, 135–157.
- (5) (a) Sutin, N. *Prog. Inorg. Chem.* **1983**, *30*, 441. (b) Marcus, R. A.; Sutin, N. *Biochim. Biophys. Acta* **1985**, *811*, 265.
- (6) Coropceanu, V.; Malagoli, M.; da Silva Filho, D. A.; Gruhn, N. E.; Bill, T. G.; Brédas, J. L. *Phys. Rev. Lett.* **2002**, *89*, 275503, 1–4.
- (7) Nelsen, S. F.; Chang, H.; Wolff, J. J.; Adamus, J. *J. Am. Chem. Soc.* **1993**, *115*, 12276–12289.
- (8) Nelsen, S. F.; Konradsson, A. E.; Weaver, M. N.; Telo, J. P. *J. Am. Chem. Soc.* **2003**, *125*, 12493–12501.
- (9) Bailey, S. E.; Zink, J. I.; Nelsen, S. F. *J. Am. Chem. Soc.* **2003**, *125*, 5939–5947.
- (10) Nelsen, S. F.; Ismagilov, R. F.; Powell, D. R. *J. Am. Chem. Soc.* **1997**, *119*, 10213–10222.
- (11) Reber, C.; Zink, J. I. *J. Phys. Chem.* **1992**, *96*, 571.
- (12) Kim Shin, K.-S.; Zink, J. I. *J. Am. Chem. Soc.* **1990**, *112*, 7148.
- (13) Reber, C.; Zink, J. I. *J. Phys. Chem.* **1992**, *96*, 571.
- (14) Bailey, S. E.; Cohan, J. S.; Zink, J. I. *J. Phys. Chem. B* **2000**, *104*, 10743.
- (15) Leng, W.; Grunden, J.; Bartholomew, G. P.; Bazan, G. C.; Myers Kelley, A. *J. Phys. Chem. A* **2004**, *108*, 10050.
- (16) Myers Kelley, A. *J. Phys. Chem. A* **1999**, *103*, 6891.
- (17) Myers, A. B. In *Laser Techniques in Chemistry*; Wiley: New York, 1995; Vol. 23, p 325.
- (18) Myers, A. B. *Chem. Rev.* **1996**, *96*, 911.
- (19) Myers, A. B. *Acc. Chem. Res.* **1997**, *30*, 519.
- (20) Lee, S.-Y.; Heller, E. J. *J. Chem. Phys.* **1979**, *71*, 4777.
- (21) Heller, E. J. *Acc. Chem. Res.* **1981**, *14*, 368.
- (22) Heller, E. J.; Sundberg, R. L.; Tannor, D. *J. Phys. Chem.* **1982**, *86*, 1822.
- (23) Zhang, J. Z.; Heller, E. J.; Huber, D.; Imre, D. G. *J. Phys. Chem.* **1991**, *95*, 6129.
- (24) Zink, J. I.; Shin, K.-S. K. In *Advances in Photochemistry*; Wiley: New York, 1991; Vol. 16, p 119.
- (25) Reber, C.; Zink, J. I. *Comments Inorg. Chem.* **1992**, *13*, 177.
- (26) Wexler, D.; Zink, J. I.; Reber, C. In *Electronic and Vibronic Spectra of Transition Metal Complexes I*; Yersin, H., Ed.; Springer-Verlag: Berlin, Heidelberg, 1994; p 174.
- (27) Simoni, E.; Reber, C.; Talaga, D.; Zink, J. I. *J. Phys. Chem.* **1993**, *97*, 12678.
- (28) Wootton, J. L.; Zink, J. I. *J. Phys. Chem.* **1995**, *99*, 7251.
- (29) Talaga, D. S.; Zink, J. I. *J. Phys. Chem.* **1996**, *100*, 8712.
- (30) Wootton, J. L.; Zink, J. I. *J. Am. Chem. Soc.* **1997**, *119*, 1895.
- (31) Neuhauser, D.; Park, T. J.; Zink, J. I. *Phys. Rev. Lett.* **2000**, *85*, 5304.
- (32) Talaga, D. S.; Zink, J. I. *J. Phys. Chem. A* **2001**, *105*, 10511.
- (33) Bailey, S. E.; Zink, J. I.; Nelsen, S. F. *J. Am. Chem. Soc.* **2003**, *125*, 5939–5947.
- (34) Bussièrre, G.; Reber, C.; Neuhauser, D.; Walter, D. A.; Zink, J. I. *J. Phys. Chem. A* **2003**, *107*, 1258–1267.
- (35) Pirsich, J. *Chem. Ber.* **1935**, *68*, 1324.
- (36) Nelsen, S. F.; Ismagilov, R. F.; Powell, D. R. *J. Am. Chem. Soc.* **1997**, *119*, 10213.
- (37) Frisch, M. J.; Trucks, G. W.; Schlegel, H. B.; Scuseria, G. E.; Robb, M. A.; Cheeseman, J. R.; Zakrzewski, V. G.; Montgomery, J. A., Jr.; Stratmann, R. E.; Burant, J. C.; Dapprich, S.; Millam, J. M.; Daniels, A. D.; Kudin, K. N.; Strain, M. C.; Farkas, O.; Tomasi, J.; Barone, V.; Cossi, M.; Cammi, R.; Mennucci, B.; Pomelli, C.; Adamo, C.; Clifford, S.; Ochterski, J.; Petersson, G. A.; Ayala, P. Y.; Cui, Q.; Morokuma, K.; Malick, D. K.; Rabuck, A. D.; Raghavachari, K.; Foresman, J. B.; Cioslowski, J.; Ortiz, J. V.; Stefanov, B. B.; Liu, G.; Liashenko, A.; Piskorz, P.; Komaromi, I.; Gomperts, R.; Martin, R. L.; Fox, D. J.; Keith, T.; Al-Laham, M. A.; Peng, C. Y.; Nanayakkara, A.; Gonzalez, C.; Challacombe, M.; Gill, P. M. W.; Johnson, B. G.; Chen, W.; Wong, M. W.; Andres, J. L.; Head-Gordon, M.; Replogle, E. S.; Pople, J. A. *Gaussian 98*, revision A.9; Gaussian, Inc.: Pittsburgh, PA, 1998.
- (38) (a) Becke, A. D. *J. Chem. Phys.* **1993**, *98*, 5648. (b) Becke, A. D. *Phys. Rev. A* **1988**, *38*, 3098. (c) Lee, C.; Yang, W.; Parr, R. G. *Phys. Rev. B* **1988**, *37*, 785. (d) Vosko, S. H.; Wilk, S. H.; Nusair, M. *Can. J. Phys.* **1980**, *58*, 1200.
- (39) Schaftenaar, G.; Noordik, J. H. Molden: A pre- and post-processing program for molecular and electronic structures. *J. Comput.-Aided Mol. Des.* **2000**, *14*, 123–134.
- (40) Alvarellos, J.; Metiu, H. *J. Phys. Chem.* **1988**, *88*, 4957.
- (41) Jiang, X. P.; Heather, R.; Metiu, H. *J. Chem. Phys.* **1989**, *90*, 6903.
- (42) Heather, R.; Metiu, H. *J. Chem. Phys.* **1992**, *96*, 2681.
- (43) Reber, C.; Zink, J. I. *J. Chem. Phys.* **1992**, *96*, 2681.
- (44) Reber, C.; Zink, J. I. *Comments Inorg. Chem.* **1992**, *13*, 177.
- (45) Wexler, D.; Reber, C.; Zink, J. I. *J. Phys. Chem.* **1992**, *96*, 8757.
- (46) Hoffman, R. *Acc. Chem. Res.* **1971**, *4*, 1.
- (47) Whangbo, M. H.; Hoffman, R. *J. Chem. Phys.* **1978**, *68*, 5498.
- (48) Reimers, J. R.; Hush, N. S. *Chem. Phys.* **1996**, *208* (2), 177–193.
- (49) Reimers, J. R.; Hush, N. S. *Chem. Phys.* **2004**, *299* (1), 79–82.
- (50) Shin, K.-S. K.; Zink, J. I. *Inorg. Chem.* **1989**, *28*, 4358.